

Geometrically nonlinear analysis of matrix cracking and delamination in composites with floating node method

Zhi, Jie; Chen, Bo Yang; Tay, Tong Earn

DOI

[10.1007/s00466-018-1591-8](https://doi.org/10.1007/s00466-018-1591-8)

Publication date

2018

Document Version

Final published version

Published in

Computational Mechanics

Citation (APA)

Zhi, J., Chen, B. Y., & Tay, T. E. (2018). Geometrically nonlinear analysis of matrix cracking and delamination in composites with floating node method. *Computational Mechanics*, 1-17.
<https://doi.org/10.1007/s00466-018-1591-8>

Important note

To cite this publication, please use the final published version (if applicable).
Please check the document version above.

Copyright

Other than for strictly personal use, it is not permitted to download, forward or distribute the text or part of it, without the consent of the author(s) and/or copyright holder(s), unless the work is under an open content license such as Creative Commons.

Takedown policy

Please contact us and provide details if you believe this document breaches copyrights.
We will remove access to the work immediately and investigate your claim.

Green Open Access added to TU Delft Institutional Repository

'You share, we take care!' - Taverne project

<https://www.openaccess.nl/en/you-share-we-take-care>

Otherwise as indicated in the copyright section: the publisher is the copyright holder of this work and the author uses the Dutch legislation to make this work public.



Geometrically nonlinear analysis of matrix cracking and delamination in composites with floating node method

Jie Zhi¹ · Bo-Yang Chen² · Tong-Earn Tay¹

Received: 13 December 2017 / Accepted: 25 May 2018 / Published online: 15 June 2018
© Springer-Verlag GmbH Germany, part of Springer Nature 2018

Abstract

In this paper, the recently-developed floating node method is extended for damage analysis of laminated composites with large deformations. Strong discontinuities including interfacial delamination and matrix cracks are explicitly represented by geometrically nonlinear kinematics. Interactions between these two kinds of failure patterns are enabled through enriched elements equipped with floating nodes. A cohesive zone model is utilized for the damage process zone. A general implicit procedure with user-defined elements is developed for both quasi-static and dynamic analysis. The performance of this formulation is verified with two benchmark simulations, involving buckling-induced delamination and low-velocity impact damage. The results presented show good quantitative and qualitative agreements with results from literature.

Keywords Large deformation · Discrete crack model · Buckling · Low velocity impact

List of symbols

\mathbf{B}	Body force per unit mass
\mathbf{B}_L	Linear strain–displacement matrix
\mathbf{d}_I	Displacements of node I in an element
\mathbf{E}	The Green–Lagrange strain
\mathbf{F}	Deformation gradient
\mathbf{F}_{coh}	Internal force vectors for cohesive elements
\mathbf{F}_{ext}	External force vectors
\mathbf{F}_{int}	Internal force vectors for solid elements
\mathbf{M}	Mass matrix
\mathbf{N}, \mathbf{n}	Normal vector of a discontinuity
\mathbf{P}	The first Piola–Kirchhoff stress
\mathbf{R}	Residual force vector
\mathbf{S}	The second Piola–Kirchhoff stress
\mathbf{T}	Traction on material boundary
\mathbf{X}, \mathbf{x}	Coordinate of a particle
\mathbb{D}	Stiffness tensor
\mathbb{R}^+	Set of positive real numbers
\mathcal{W}	Work

J	Determinant, $\det \mathbf{F}$
K	Penalty stiffness of the cohesive element
L_I	Shape function of node I in a cohesive element
N_I	Shape function of node I in a solid element
n_{el_c}	Number of cohesive elements
n_{el_s}	Number of solid elements
n_{nd_c}	Number of nodes in a cohesive element
n_{nd_s}	Number of nodes in a solid element

Greek characters

σ	Cauchy stress
φ	Deformation map
Γ	Discontinuous surface or interface
Ω	Domain in the physical space
ω	Damage variable
$\partial_t \Omega$	Traction boundary
$\partial_u \Omega$	Displacement boundary

Sub/superscripts

\square^e	Related to a finite element
$\square^{(i)}$	Related to $\Omega^{(i)}$, $i = 1, 2$
\square^α	Related to Γ^α , $\alpha = +, -$
\square_0	With respect to reference configuration
\square_n, \square_t	Normal and tangential components, respectively
\square_s, \square_c	Related to solid elements and cohesive elements, respectively

✉ Jie Zhi
jie.zhi@u.nus.edu

¹ Department of Mechanical Engineering, National University of Singapore, 21 Lower Kent Ridge Road, Singapore 119077, Singapore

² Faculty of Aerospace Engineering, Delft University of Technology, 2629 HS Delft, Netherlands

Operators

\mathbf{A}	\square	Assembly operator for finite elements
$\square \otimes \square$		Nonstandard dyadic product, $\square_{ijkl} = \square_{ik} \square_{jl}$
$\square \otimes \square$		Dyadic product
$\langle \square \rangle$		Macauley bracket
$\llbracket \square \rrbracket$		Jump of a function over a discontinuity in its domain
Grad	\square	Gradient with respect to reference configuration
$\{\square\}$		Voigt notation
$L[\square]$		Linearization of a nonlinear function

1 Introduction

With extensive application of composite laminate materials in aeronautical, automotive and civil industries, understanding the failure mechanisms of composites becomes critical for the virtual testing of engineering products [1,2]. While composite structures are reinforced in the fiber direction, damage and fracture usually initiates from weaker regions including fiber/matrix interfaces [3], manufacturing defects/statistical inhomogeneities within ply materials [4] and interfaces between plies with different orientations [5], which can further develop into matrix cracking and delamination. As a result, residual strength can be significantly reduced by these sub-critical damage patterns, for example Barely Visible Impact Damage (BVID) due to low velocity impact [6,7]. The simulation of damage evolution within the context of computational procedures involves highly nonlinear processes and remains challenging [8].

The localized failure of quasi-brittle solids is usually attributed to dominant cracks linked up by several small cracks and can be characterized with inelastic softening models. In finite element modeling, the existing approaches can be classified into two broad categories, the continuous approach (*smearred crack model*) and the discontinuous approach (*discrete crack model*) [9]. In the first approach, typically, a stress-based constitutive relation is developed with continuum damage mechanics and the effect of discontinuity is smeared out over the continuum. However, this method, also sometimes known as material property degradation, suffers from mesh dependence due to the loss of well-posedness of the boundary value problem and potentially spurious stress transfer [10]. Several techniques such as non-local or gradient enhancement [11,12] have been proposed to overcome these shortcomings. Recently, an alternative class for continuum descriptions of cracks called phase field methods has been developed based on variation theory of fracture [13–15]. With zero-width discontinuities regularized into diffuse entities, complex crack behaviour could be handled without relying on local criteria. However, rather fine discretization is generally still

required to account for the small length scales at the localization zone, unless adaptive mesh refinement is used [16,17]. In any case, they are fundamentally unable to deal with the strong displacement discontinuities of physical cracks.

The second approach resolves the propagation of discontinuities with explicit representation of crack kinematics in spatial discretization based on enrichment of continuous solution space in standard finite elements. A traction-based constitutive relation, in the context of a *cohesive zone model* (CZM), is usually used to model the damage process zone [18]. Enriched degrees of freedom, either for elements or nodes, are termed as XFEM or XFEM, respectively [19]. Another equivalent formulation to XFEM is the *phantom node method* (PNM) [20]. As illustrated in Fig. 1, the same number of total DOFs is used for XFEM and PNM but the parametrization of displacement jump within elements is different [21]. The displacement field in XFEM is decomposed into continuous part with u_2, u_3 and discontinuous part with $\llbracket u \rrbracket_2, \llbracket u \rrbracket_3$ while that in PNM for two internal domains is reproduced from two independent overlapping paired elements with nodal displacement u_2, u_3^* and u_2^*, u_3 . The advantage of PNM in treating non-additive nodal degrees of freedom makes it popular in various applications [22–24] including finite deformation settings [25–28].

While the *smearred crack model* has been well documented for progressive damage modeling of composites [29–31], *discrete crack models* have been receiving more attention recently. Van der Meer et al. [32] proposed a phantom node formulation with mixed mode cohesive law for splitting in laminates, investigated the interaction between discrete matrix cracking and delamination [33], and integrated additionally a continuum damage model for the study of complex failure mechanisms observed in open-hole tests and compact tension tests [34]. A discontinuous solid-like shell element was developed for the simulation of progressive failure in laminated composites under transverse loading [35]. Yang et al. presented an augmented finite element method, a variant of PNM, for coupled transverse intra-ply cracks and delamination cracks in composites [36,37], and also an augmented cohesive element for crack bifurcation and coalescence [38], with which high-fidelity simulations of multiple fracture processes in a double-notched tension specimen were achieved [39]. Tay et al. [40] proposed a XFEM-CE (extended-FEM cohesive element) approach for modeling delamination, matrix cracks and their interactions in progressive failure of composite laminates and studied the phenomenon of delamination migration in multi-directional laminates [41]. Chen et al. [42] proposed the floating node method (FNM) for modeling multiple discontinuities. The idea of “floating nodes” introduces extra nodes with no pre-assigned nodal position vectors, but which may be subsequently deployed to define

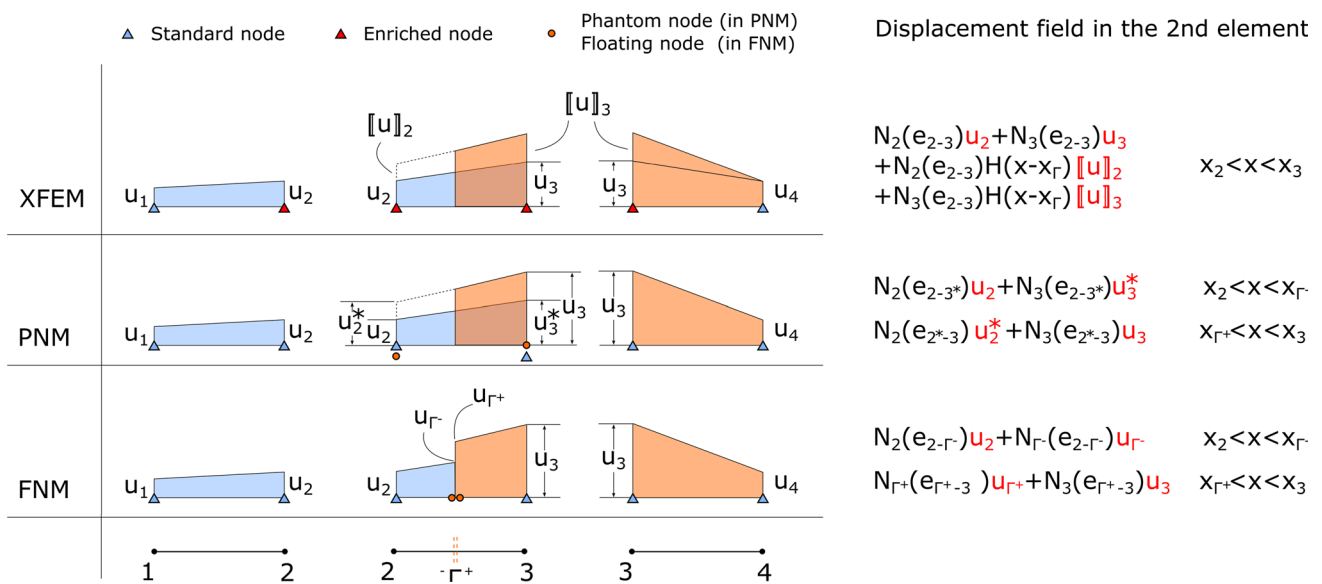


Fig. 1 Illustrations of XFEM, PNM and FNM with three 1D elements and discontinuity in the 2nd element (‘Standard node’ is the node as in standard FE with 1 DOF; ‘Enriched node’ is the node with 2 DOFs; ‘Phantom node’ or ‘Floating node’ is the extra node with 1 DOF; N

is the shape function, e.g., $N_2(e_{2-3})$ is the shape function of node 2 within element composed of node 2 & 3; x is the coordinate; $H(x)$ is the Heaviside function)

boundaries of discontinuities or cracks as determined by fracture or damage criteria. Instead of using overlapping domains in PNM, the crack is tracked geometrically with floating nodes (nodal displacement u_{Γ^-} , u_{Γ^+}) as shown in Fig. 1. An advantage of FNM is that it eliminates errors associated with the mapping of straight cracks in PNM from physical to natural coordinates, making it more suitable for representing complex crack networks [42]. The complete tensile failure process of laminated composites and delamination migration in angle-ply laminates were successfully modeled with FNM [43,44]. The coupled failure mechanisms including matrix cracking (transverse matrix cracks or longitudinal splittings) and delamination have also been studied with other similar methods, refined XFEM [45–47], extended cohesive damage method [48], extended layerwise method [49], among others.

Current developments in *discrete crack models* for damage and fracture of composites are mostly limited to linear problems [34,39,42]. However, many important problems involve large displacements and rotations, such as those involving buckling or post-buckling failure and impact or ballistic damage. A combination of buckling and delamination was simulated by Qiu et al. [50] with geometric non-linearity formulated in a co-rotational framework. Reinoso et al. [51] developed a nonlinear finite thickness cohesive element based on solid shell concept for delamination in composite laminates. Comparisons between linear and nonlinear formulations were discussed and the necessity of incorporation of geometrically nonlinear effects was verified in a recent work by Škec and Jelenić [52]. However, these methods are

not readily applicable to a general problem with both matrix cracking and delamination process [38,45]. Thus, this paper aims at further extending the formulation of FNM for geometrically nonlinear analyses.

The structure of this paper is organized as follows. In Sect. 2, the kinematics of matrix cracking and delamination are firstly derived. The contributions of bulk materials and damage process zone in principle of virtual work and corresponding material models are given. The discretization formulations are shown in Sect. 3, where enriched solid elements and enriched interface elements with FNM are presented. Section 4 addresses the numerical implementation issues. Two numerical examples are shown in Sect. 5 and conclusions are drawn in Sect. 6.

2 Finite deformation analysis of strong discontinuities in matrix cracking and delamination

We present in this section the kinematic equations for incorporating strong discontinuities for both matrix cracks and delamination, the derivation of which follows the work by Mergheim and Steinmann [27]. Governing equations, including equilibrium equations and constitutive laws, are elaborated for a two-dimensional boundary value problem containing cohesive cracks.

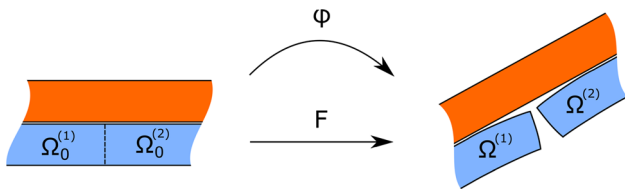


Fig. 2 Kinematics of strong discontinuity (matrix cracking)

2.1 Kinematics

In finite deformation problems, the motion and deformation of a continuum body are usually defined in a reference configuration $X \in \Omega_0$ and a current configuration $x \in \Omega$. A one-to-one mapping is defined as $x = \varphi(X, t)$, $\varphi : \Omega_0 \times \mathbb{R}^+ \rightarrow \Omega$. To describe the deformation locally, a tangent map $dx = F dX$ is introduced where $F = \text{Grad } \varphi$ is deformation gradient and its determinant is denoted by J .

Suppose a matrix crack divides the body Ω into two disjoint parts $\Omega^{(1)}$ and $\Omega^{(2)}$ and a virtual crack exists in the reference configuration, as shown in Fig. 2. To incorporate the discontinuity in the deformation map, the *Heaviside* function can be introduced [25,53]. But a simpler definition following Mergheim and Steinmann [27] is given here

$$\varphi = \begin{cases} \varphi^{(1)}(X) : \Omega_0^{(1)} \rightarrow \Omega^{(1)} \\ \varphi^{(2)}(X) : \Omega_0^{(2)} \rightarrow \Omega^{(2)} \end{cases} \quad (1)$$

which means deformation gradient and other kinematics can be defined independently for $\Omega_0^{(1)}$ and $\Omega_0^{(2)}$:

$$F = \begin{cases} F^{(1)} = \text{Grad } \varphi^{(1)} & \text{in } \Omega_0^{(1)} \\ F^{(2)} = \text{Grad } \varphi^{(2)} & \text{in } \Omega_0^{(2)} \end{cases} \quad (2)$$

with corresponding determinants $J^{(1)}$ and $J^{(2)}$.

For the generated discontinuity or interface between layers, the surface Γ_0 can be mapped to different parts Γ^+ and Γ^- under two independent deformation maps φ^+ and φ^- . A jump of the deformation map between two surfaces is given by

$$[[\varphi]] = \varphi^+ - \varphi^- \quad (3)$$

which also implies the displacement jump $[[u]] = [[\varphi]]$. For the convenience of defining discontinuous behavior, a fictitious surface $\bar{\Gamma}$ (Fig. 3) is introduced with the average map

$$\bar{\varphi} = \frac{1}{2}[\varphi^+ + \varphi^-] : \Gamma_0 \rightarrow \bar{\Gamma}. \quad (4)$$

Deformation gradient is then defined as $\bar{F} = \text{Grad } \bar{\varphi}$ and $\bar{J} = \det(\bar{F})$. The normal vector n of this fictitious surface relates

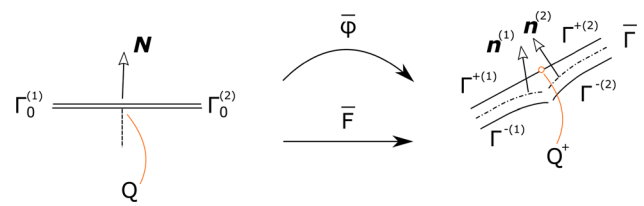


Fig. 3 Kinematics of interface (delamination)

to referential normal vector N through *Nanson’s* formula

$$n = \frac{\bar{F}^{-T} \cdot N}{|\bar{F}^{-T} \cdot N|}. \quad (5)$$

An important feature of damage in laminates is the interaction between matrix cracking and delamination, as illustrated in Fig. 2, which shows the coalescence of intra- and inter-layer cracks. Suppose the interface is broken at point Q and this point separates the fictitious surface $\bar{\Gamma}$ into $\bar{\Gamma}^{(1)}$ and $\bar{\Gamma}^{(2)}$ (Fig. 3). Similar deformation map as Eq. (1) is given as

$$\bar{\varphi} = \begin{cases} \bar{\varphi}^{(1)}(X) : \Gamma_0^{(1)} \rightarrow \bar{\Gamma}^{(1)} \\ \bar{\varphi}^{(2)}(X) : \Gamma_0^{(2)} \rightarrow \bar{\Gamma}^{(2)} \end{cases} \quad (6)$$

with deformation gradient

$$\bar{F} = \begin{cases} \bar{F}^{(1)} = \text{Grad } \bar{\varphi}^{(1)} & \text{in } \Gamma_0^{(1)} \\ \bar{F}^{(2)} = \text{Grad } \bar{\varphi}^{(2)} & \text{in } \Gamma_0^{(2)} \end{cases}. \quad (7)$$

$\Gamma_0^{(1)}$ and $\Gamma_0^{(2)}$ denote two disjoint parts of the interface in the initial configuration, which is cut by a virtual matrix crack. The relationship between $n^{(i)}$ ($i = 1, 2$) and N are defined by Eq. (5) with $\bar{F}^{(i)}$ ($i = 1, 2$), where the superscript “ (i) ” refers to different parts of the interface.

2.2 Equilibrium equation

Considering a typical boundary value problem, a solid Ω with displacement boundary $\partial_u \Omega$, traction boundary $\partial_t \Omega$ and cohesive cracks Γ , the local balance equations and boundary conditions with respect to the reference configuration are expressed as

$$\begin{aligned} \text{DIV } P + \rho_0 B &= \rho_0 \ddot{u} && \text{in } \Omega_0 \setminus \Gamma_0 \\ u &= \hat{u} && \text{on } \partial_u \Omega_0 \\ P \cdot N &= \hat{T} && \text{on } \partial_t \Omega_0 \\ P \cdot N^- &= -P \cdot N^+ = T_c && \text{on } \Gamma_0 \end{aligned} \quad (8)$$

where P is the first *Piola–Kirchhoff* stress, B is the body force per unit mass and T_c is the cohesive traction. For the sake of simplicity, we treat interface layer and

solution-dependent discontinuity surface uniformly as cohesive cracks.

The first of Eq. (8) is satisfied in a weak sense by weighted integration over the domain with a test function $\delta \mathbf{u}$, which vanishes at the *Dirichlet* boundary. The weak formulation with discontinuity surface [54] is given as

$$\int_{\Omega_0 \setminus \Gamma_0} \mathbf{P} : \text{Grad } \delta \mathbf{u} \, dV + \int_{\Gamma_0} \mathbf{T}_c \cdot \llbracket \delta \mathbf{u} \rrbracket \, dA = \int_{\Omega_0 \setminus \Gamma_0} \rho_0 (\mathbf{B} - \ddot{\mathbf{u}}) \cdot \delta \mathbf{u} \, dV + \int_{\partial_t \Omega_0} \hat{\mathbf{T}} \cdot \delta \mathbf{u} \, dA \tag{9}$$

Replacing \mathbf{P} by the second Piola–Kirchhoff stress \mathbf{S} through $\mathbf{P} = \mathbf{F} \cdot \mathbf{S}$, we obtain $\mathbf{P} : \text{Grad } \delta \mathbf{u} = \mathbf{S} : \delta \mathbf{E}$, where \mathbf{E} is Green–Lagrange strain. Eq. (9) can then be interpreted as the principle of virtual work, which is written in the total Lagrangian formulation

$$\delta \mathcal{W} = \delta \mathcal{W}_{\text{kin}} + \delta \mathcal{W}_{\text{int}} + \delta \mathcal{W}_{\text{coh}} - \delta \mathcal{W}_{\text{ext}} = 0 \tag{10}$$

where

$$\begin{aligned} \delta \mathcal{W}_{\text{kin}} &= \int_{\Omega_0 \setminus \Gamma_0} \rho_0 \ddot{\mathbf{u}} \cdot \delta \mathbf{u} \, dV \\ \delta \mathcal{W}_{\text{int}} &= \int_{\Omega_0 \setminus \Gamma_0} \mathbf{S} : \delta \mathbf{E} \, dV \\ \delta \mathcal{W}_{\text{coh}} &= \int_{\Gamma_0} \mathbf{T}_c \cdot \llbracket \delta \mathbf{u} \rrbracket \, dA \\ \delta \mathcal{W}_{\text{ext}} &= \int_{\Omega_0 \setminus \Gamma_0} \rho_0 \mathbf{B} \cdot \delta \mathbf{u} \, dV + \int_{\partial_t \Omega_0} \hat{\mathbf{T}} \cdot \delta \mathbf{u} \, dA \end{aligned} \tag{11}$$

The cohesive term can be rewritten in the current configuration through $\mathbf{T}_c \, dA = \mathbf{t}_c \, da$ if *Cauchy* traction is used in the constitutive law.

2.3 Material models

The constitutive equations are defined to describe the material response of composites with elastic behavior for bulk layers and cohesive behavior for matrix cracks or interfaces between layers. For applications with large displacements but small strains, linear constitutive equations [55,56] are given as

$$\mathbf{S} = \mathbb{D} : \mathbf{E} \tag{12}$$

and the matrix form of compliance $\mathbb{C} = \mathbb{D}^{-1}$ is

$$\mathbb{C} = \begin{bmatrix} \frac{1}{E_1} & -\frac{\nu_{21}}{E_2} & -\frac{\nu_{31}}{E_3} & 0 & 0 & 0 \\ -\frac{\nu_{12}}{E_1} & \frac{1}{E_2} & -\frac{\nu_{32}}{E_3} & 0 & 0 & 0 \\ -\frac{\nu_{13}}{E_1} & -\frac{\nu_{23}}{E_2} & \frac{1}{E_3} & 0 & 0 & 0 \\ 0 & 0 & 0 & \frac{1}{G_{12}} & 0 & 0 \\ 0 & 0 & 0 & 0 & \frac{1}{G_{13}} & 0 \\ 0 & 0 & 0 & 0 & 0 & \frac{1}{G_{23}} \end{bmatrix} \tag{13}$$

where the *Poisson’s* ratios satisfy

$$\frac{\nu_{ij}}{E_i} = \frac{\nu_{ji}}{E_j} \tag{14}$$

Thus, a total of nine engineering constants are required for Eq. (13).

To evaluate the fracture of quasi-brittle materials under tension (e.g., matrix cracking in 90° plies), the *Rankine* criterion based on principal stress is adopted [21]. The spectral decomposition of a 2D *Cauchy* stress gives

$$\boldsymbol{\sigma} = \lambda_1 \mathbf{n}_1 \otimes \mathbf{n}_1 + \lambda_2 \mathbf{n}_2 \otimes \mathbf{n}_2 \tag{15}$$

When $\max(\lambda_1, \lambda_2) = \lambda_i > f_n$ (f_n is the tensile strength), the corresponding eigenvector \mathbf{n}_i determines the crack direction. According to *Nanson’s* formula, the virtual crack direction in the reference configuration can be determined by

$$\mathbf{N}_i = \frac{\mathbf{F}^T \cdot \mathbf{n}_i}{|\mathbf{F}^T \cdot \mathbf{n}_i|} \tag{16}$$

The constitutive behavior of the discontinuity surface in a typical cohesive formulation is generally defined between traction \mathbf{t} and separation $\llbracket \mathbf{u} \rrbracket$. We assume in this work that the displacement discontinuities are small in the non-fully opened surfaces, following the work by Allix and Corigliano [57]. Therefore, a mixed-mode cohesive law based on a deformation driven damage model, which was developed by Turon et al. [58] and later implemented in applications [59] with geometrically nonlinear effects, is adopted here.

In this model, a bi-linear relation between normal component and tangential component of traction and separation is used. The normal and tangential separations are given by

$$\begin{aligned} \llbracket \mathbf{u} \rrbracket_n &= (\llbracket \mathbf{u} \rrbracket \cdot \mathbf{n}) \\ \llbracket \mathbf{u} \rrbracket_t &= \llbracket \mathbf{u} \rrbracket - (\llbracket \mathbf{u} \rrbracket \cdot \mathbf{n}) \mathbf{n} \end{aligned} \tag{17}$$

where \mathbf{n} is the normal vector of the fictitious surface. Traction can be defined independently as

$$\begin{aligned} \mathbf{t}_n &= (1 - \omega) K \llbracket \mathbf{u} \rrbracket_n - \omega K \langle -\llbracket \mathbf{u} \rrbracket \cdot \mathbf{n} \rangle \mathbf{n} \\ \mathbf{t}_t &= (1 - \omega) K \llbracket \mathbf{u} \rrbracket_t \end{aligned} \tag{18}$$

where ω is a scalar damage variable ($0 \leq \omega \leq 1$), K is a penalty stiffness and $\langle \square \rangle = (\square + |\square|)/2$ is the *Macaulay* bracket. A damage loading function is defined as

$$f(\lambda, r) = \lambda - r \tag{19}$$

where $\lambda = \sqrt{\langle \llbracket \mathbf{u} \rrbracket \cdot \mathbf{n} \rangle^2 + \|\llbracket \mathbf{u} \rrbracket_s\|^2}$ is an equivalent separation and r is the current damage threshold (r^o denotes the initial value), the update of which is generally formalized in the *Kuhn-Tucker* loading-unloading condition

$$f \leq 0, \dot{r} \geq 0, f\dot{r} = 0. \tag{20}$$

The damage formulation is completed by an evolution law

$$\dot{\omega} = \frac{\Delta^f (r - \Delta^o)}{r(\Delta^f - \Delta^o)} \tag{21}$$

where the onset separation $\Delta^o = r^o$ and the final separation Δ^f can be obtained from damage initial criterion and the B–K fracture criterion [58].

3 FE formulation of the floating node method

The weak formulation shown in the previous section is discretized with the standard finite element method for the boundary value problem with cohesive cracks. The FE formulations of enriched ply elements and enriched interface elements are developed with FNM for matrix cracking and delamination, respectively.

3.1 Standard FE formulation

The discrete formulation starts with the approximation of the original domain Ω_0 (bulk part $\Omega_0 \setminus \Gamma_0$ and interface part Γ_0) as the union of n_{el_s} solid elements and n_{el_c} cohesive elements

$$\begin{aligned} \Omega_0 \setminus \Gamma_0 &\approx \bigcup_{e=1}^{n_{el_s}} \Omega_0^e, \\ \Gamma_0 &\approx \bigcup_{e=1}^{n_{el_c}} \Gamma_0^e \end{aligned} \tag{22}$$

where the discretization of Γ_0 here only includes interface layer since the location of discontinuity surface is only known on the fly during the simulation. Similarly, the boundary is discretized as $\partial_u \Omega_0^e$ and $\partial_t \Omega_0^e$.

In a solid element Ω^e , the geometric (\mathbf{X} and \mathbf{x}) and kinematic variables are interpolated with isoparametric shape functions and nodal values. The displacement and deformation gradient within this element are written as

$$\begin{aligned} \mathbf{u}^e &= \sum_{I=1}^{n_{nd_s}} N_I^e \mathbf{d}_I^e, \\ \mathbf{F}^e &= \sum_{I=1}^{n_{nd_s}} \mathbf{x}_I^e \otimes \nabla_X N_I^e \end{aligned} \tag{23}$$

where \mathbf{d}_I^e , \mathbf{x}_I^e denote the I -th nodal displacement, coordinate in the e -th element, respectively. N_I^e is corresponding shape function and n_{nd_s} is the number of nodes in the solid element.

Similar definitions of interpolation are given for cohesive element Γ^e , where two paired surfaces $(\Gamma^e)^+$ and $(\Gamma^e)^-$ are identified similarly in Fig. 3. With the formula in Eq. (23) known for the bulk solid, the displacement of these two paired surfaces can also be derived. Therefore, the displacement jump between two surfaces is given as

$$\llbracket \mathbf{u} \rrbracket^e = \sum_{I=1}^{n_{nd_c}} L_I^e \mathbf{d}_I^e \tag{24}$$

where n_{nd_c} is the number of nodes in the cohesive element and L_I^e is the shape function of the cohesive element

$$L_I^e = \begin{cases} \bar{N}_I^e, & \text{node } I \in (\Gamma^e)^+ \\ -\bar{N}_I^e, & \text{node } I \in (\Gamma^e)^- \end{cases} \tag{25}$$

where \bar{N}_I^e is the shape function degenerated by N_I^e on the surface. For example, if N is the shape function of a four-node plane element, \bar{N} is the shape function of a two-node line element. Then the deformation gradient associated with the average map (Eq. 4) in cohesive element is given by

$$\bar{\mathbf{F}}^e = \frac{1}{2} \sum_{I=1}^{n_{nd_c}} \mathbf{x}_I^e \otimes \nabla_X \bar{N}_I^e. \tag{26}$$

The variation of *Green–Lagrange* strain is given by

$$\delta \mathbf{E}^e = \frac{1}{2} \sum_{I=1}^{n_{nd_s}} [\mathbf{F}^{eT} \cdot (\delta \mathbf{x}_I^e \otimes \nabla_X N_I^e) + (\nabla_X N_I^e \otimes \delta \mathbf{x}_I^e) \cdot \mathbf{F}^e] \tag{27}$$

the *Voigt* notation of which is

$$\{\delta \mathbf{E}^e\} = \sum_{I=1}^{n_{nd_s}} (\mathbf{B}_L^e)_I \delta \mathbf{x}_I^e. \tag{28}$$

For a detailed formulation of \mathbf{B}_L^e , refer to [60].

Substituting Eqs. (23), (24), (26) and (27) into Eq. (10), we obtain

$$\delta \mathbf{d}^T \mathbf{R} = 0 \implies \mathbf{R} = \mathbf{A}(\mathbf{R}_s, \mathbf{R}_c) = \mathbf{0} \tag{29}$$

where \mathbf{A} is an assembly operator and \mathbf{R}_s and \mathbf{R}_c are residual vectors contributed from solid elements and cohesive elements given by (neglecting body force)

$$\mathbf{R}_s = \mathbf{A}_{e=1}^{n_{el_s}} \left(\underbrace{\int_{\Omega_0^e} \rho_0 \mathbf{N}^{eT} \mathbf{N}^e dV \ddot{\mathbf{d}}^e}_{\mathbf{M}^e} + \underbrace{\int_{\Omega_0^e} \mathbf{B}_L^{eT} \{\mathbf{S}\} dV}_{\mathbf{F}_{int}^e} - \underbrace{\int_{\partial_i \Omega_0^e} \mathbf{N}^{eT} \hat{\mathbf{T}} dA}_{\mathbf{F}_{ext}^e} \right) \quad (30)$$

and

$$\mathbf{R}_c = \mathbf{A}_{e=1}^{n_{el_c}} \left(\underbrace{\int_{\Gamma^e} \mathbf{L}^{eT} \mathbf{t}_c da}_{\mathbf{F}_{coh}^e} \right) \quad (31)$$

where $(\mathbf{N}^e)_I = \mathbf{N}_I^e \mathbf{I}_2$ ($I = 1, 2, \dots, n_{nd_s}$) and $(\mathbf{L}^e)_I = \mathbf{L}_I^e \mathbf{I}_2$ ($I = 1, 2, \dots, n_{nd_c}$), \mathbf{I}_2 is the identity matrix. Although a consistent form is presented here for the mass matrix \mathbf{M}^e , the lumped mass matrix is usually used in practice for efficiency. For 2D problems, quadrilateral-type elements are used for both solid and cohesive elements with node number $n_{nd_s} = n_{nd_c} = 4$.

3.2 Enriched solid elements

When crack initiates in or propagates through the solid element, the quadrilateral element is split into two parts, either two quadrilateral elements or one triangular element and pentagonal element. Take the first scenario as an example, the original domain Ω^e is then divided into two solid parts and one cohesive part $\Omega^e = \Omega^{e(1)} \cup \Omega^{e(2)} \cup \Gamma^e$, as shown in Fig. 4. Similar with Eq. (1), the deformation map can be defined independently for these three parts

$$\boldsymbol{\varphi}^e = \begin{cases} \boldsymbol{\varphi}^{e(1)}(\mathbf{X}) & : \Omega_0^{e(1)} \rightarrow \Omega^{e(1)} \\ \boldsymbol{\varphi}^{e(2)}(\mathbf{X}) & : \Omega_0^{e(2)} \rightarrow \Omega^{e(2)} \\ \bar{\boldsymbol{\varphi}}^e(\mathbf{X}) & : \Gamma_0^e \rightarrow \Gamma^e \end{cases} \quad (32)$$

which means that the corresponding deformation gradients, strains and stresses may be defined separately within $\Omega^{e(1)}$, $\Omega^{e(2)}$ and Γ^e . Note that a virtual crack can be defined in the reference configuration for the definition of $\Omega_0^{e(1)}$, $\Omega_0^{e(2)}$ and Γ_0^e .

Based on the concept of floating node [42], extra DOFs are introduced into the original element. Two nodes per cracked edge are placed directly where crack and edges intersect.

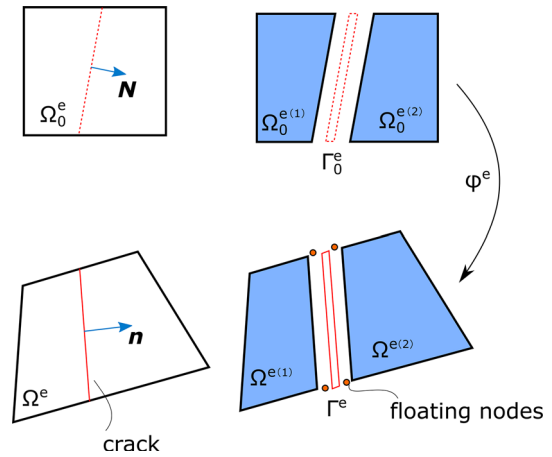


Fig. 4 The enriched solid element with independent deformation maps

An advantage over the PNM, which also introduces new DOFs at existing nodes, is that standard element formulation including shape function and integration scheme can be adopted. In another words, the enriched solid element is actually equivalent to two solid elements and one cohesive element. Therefore, the discrete residual statement of the enriched solid element is given by

$$\mathbf{R}_{ers}^e = \mathbf{A}(\mathbf{R}_s^e|_{\Omega_0^{e(1)}}, \mathbf{R}_s^e|_{\Omega_0^{e(2)}}, \mathbf{R}_c^e|_{\Gamma^e}) \quad (33)$$

where \mathbf{R}_s^e and \mathbf{R}_c^e are discrete residuals of standard solid element and cohesive element as given by Eqs. (30) and (31), $\square|_*$ denotes the integral domain. Note that the formulation for the other scenario is similar except that one triangular element and one pentagonal element (consists of three triangular elements) are used as the equivalent.

3.3 Enriched interface elements

With the crack reaching the edge of interface, interaction between matrix cracking and delamination can be considered with an enriched interface element, as shown in Fig. 5. Suppose the crack cut the bottom of the interface element and the domain is divided as $\bar{\Gamma}^e = \bar{\Gamma}^{e(1)} \cup \bar{\Gamma}^{e(2)}$. The deformation map can be defined as

$$\bar{\boldsymbol{\varphi}}^e = \begin{cases} \bar{\boldsymbol{\varphi}}^{e(1)}(\mathbf{X}) & : \Gamma_0^{e(1)} \rightarrow \bar{\Gamma}^{e(1)} \\ \bar{\boldsymbol{\varphi}}^{e(2)}(\mathbf{X}) & : \Gamma_0^{e(2)} \rightarrow \bar{\Gamma}^{e(2)} \end{cases} \quad (34)$$

Two floating nodes are introduced at the cracked edge while only one is placed at the other intact edge. The enriched interface element can then be formulated as an assembly of two cohesive elements

$$\mathbf{R}_{erc}^e = \mathbf{A}(\mathbf{R}_c^e|_{\bar{\Gamma}^{e(1)}}, \mathbf{R}_c^e|_{\bar{\Gamma}^{e(2)}}). \quad (35)$$

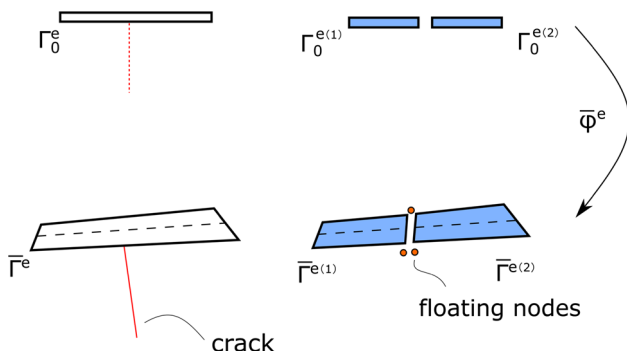


Fig. 5 The enriched cohesive element with independent deformation maps

4 Numerical implementation

The numerical implementation of the aforementioned formulation is outlined in this section.

4.1 Solution of the boundary value problem

Recalling the discrete residual statements given by Eqs. (30), (31), (33) and (35), we can write them in a compact form

$$M\ddot{\mathbf{d}} + \mathbf{F}_{\text{int}}(\mathbf{d}) + \mathbf{F}_{\text{coh}}(\mathbf{d}) - \mathbf{F}_{\text{ext}} = \mathbf{0}. \tag{36}$$

where M is the global mass matrix and F are global force vector (F_{int} and F_{ext} are the internal force and the external force contributed from solid elements, respectively; F_{coh} is the internal force from cohesive elements). To solve this dynamic problem, implicit time integration is implemented with the *Hilber–Hughes–Taylor* (HHT) operator [61], a generalization of *Newmark* operator with controllable numerical damping. Instead of Eq. (36), the equation to be solved at a solution time step t_{n+1} may be given as

$$\mathbf{R}(\mathbf{d}_{n+1}) = M\ddot{\mathbf{d}}_{n+1} + (1 + \alpha)[\mathbf{F}_{\text{int}}(\mathbf{d}_{n+1}) + \mathbf{F}_{\text{coh}}(\mathbf{d}_{n+1}) - \mathbf{F}_{\text{ext},n+1}] - \alpha[\mathbf{F}_{\text{int}}(\mathbf{d}_n) + \mathbf{F}_{\text{coh}}(\mathbf{d}_n) - \mathbf{F}_{\text{ext},n}] = \mathbf{0} \tag{37}$$

The displacements and velocities at t_{n+1} are computed by the *Newmark* formula

$$\mathbf{d}_{n+1} = \mathbf{d}_n + \Delta t \dot{\mathbf{d}}_n + \Delta t^2 \left[\left(\frac{1}{2} - \beta \right) \ddot{\mathbf{d}}_n + \beta \ddot{\mathbf{d}}_{n+1} \right], \tag{38}$$

$$\dot{\mathbf{d}}_{n+1} = \dot{\mathbf{d}}_n + \Delta t \left[(1 - \gamma) \ddot{\mathbf{d}}_n + \gamma \ddot{\mathbf{d}}_{n+1} \right]. \tag{39}$$

Rearranging Eq. (38), we obtain the expression for $\ddot{\mathbf{d}}_{n+1}$

$$\ddot{\mathbf{d}}_{n+1} = \frac{1}{\beta \Delta t^2} (\mathbf{d}_{n+1} - \mathbf{d}_n) - \frac{1}{\beta \Delta t} \dot{\mathbf{d}}_n - \left(\frac{1}{2\beta} - 1 \right) \ddot{\mathbf{d}}_n. \tag{40}$$

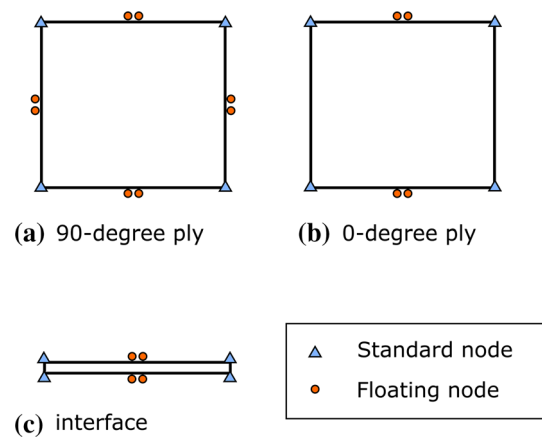


Fig. 6 Standard nodes and floating nodes within three types of elements

where $\beta = 0.25(1 - \alpha)^2$, $\gamma = 0.5 - \alpha$ and $-0.5 \leq \alpha \leq 0$. α is a parameter controlling the amount of numerical damping [62].

Substituting $\ddot{\mathbf{d}}_{n+1}$ back into Eq. (37), we have \mathbf{d}_{n+1} as the only unknown variable. Generally, $\mathbf{R}(\mathbf{d}_{n+1})$ is a non-linear function which requires solution by *Newton-Raphson* iterations. The linearization of \mathbf{R} may be computed as

$$\mathbf{R}(\mathbf{d}_{n+1}^{(k)}) + \frac{\partial \mathbf{R}}{\partial \mathbf{d}} \Big|_{\mathbf{d}_{n+1}^{(k)}} \Delta \mathbf{d}_{n+1}^{(k+1)} = \mathbf{0} \tag{41}$$

where (k) denotes iteration number and the tangent stiffness matrix is given by

$$\frac{\partial \mathbf{R}}{\partial \mathbf{d}} = \frac{M}{\beta \Delta t^2} + (1 + \alpha) \left(\frac{\partial \mathbf{F}_{\text{int}}}{\partial \mathbf{d}} + \frac{\partial \mathbf{F}_{\text{coh}}}{\partial \mathbf{d}} \right) \tag{42}$$

where the sum of second and third terms on the right-hand side is the tangent matrix due to the linearization of internal and cohesive forces, respectively. Details at the element level are presented in “Appendix”. After the solution of Eq. (41), the displacements can be updated as $\mathbf{d}_{n+1}^{(k+1)} = \mathbf{d}_{n+1}^{(k)} + \Delta \mathbf{d}_{n+1}^{(k+1)}$. The velocity and acceleration are obtained with Eqs. (39) and (40), respectively. This process is iterated until convergence before the start of the next time step. Note that the inertial term can be ignored and standard *Newton-Raphson* method is adopted for solving a quasi-static problem.

4.2 Specific implementation details

Details on the implementation of the FNM for modeling laminates with interfaces have been addressed in previous work [42,43]. In this paper, we formulate the implementation for 2D problems, such as unidirectional laminates and cross-ply laminates. Three types of enriched elements are developed

Fig. 7 Scenarios of crack propagation in a mesh **a** two 90° ply elements; **b** one interface element and one 0° ply element

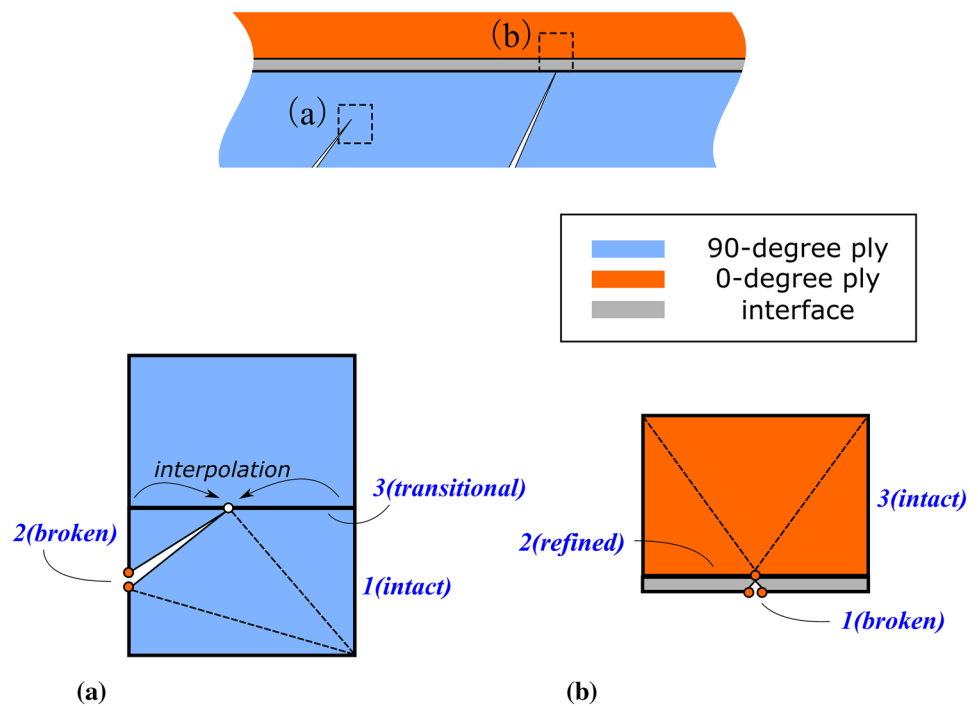
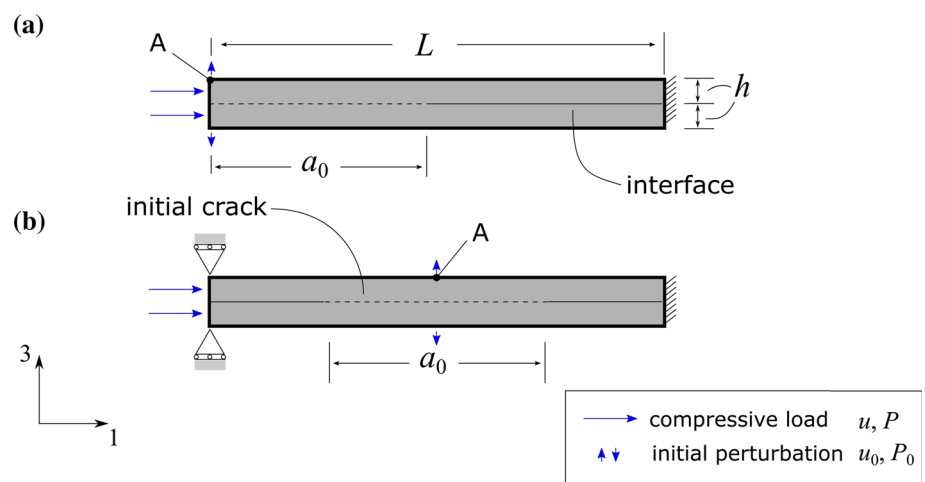


Fig. 8 Compressed composite beam with initial cracks and symmetrical perturbations **a** Case-1; **b** Case-2



for 90°, 0° plies and interface layers, respectively. As illustrated in Fig. 6, besides standard FE nodes, floating nodes in solid elements and cohesive elements are associated with edges which may potentially break or require remeshing. Note that although the floating nodes are predefined in the elements, they are only activated when the element is cut by a crack.

In the current model, each continuous crack consists of cohesive segments within several solid elements and the simulation of crack propagation is achieved with edge status variable approach [43], which tracks whether a particular edge is cracked or not. During fracture, it is assumed that the crack tip propagates from one edge to another in an element. Therefore, only the local status information of each edge is

Table 1 Parameters (Geometric dimensions and material properties) of the beam [57]

Parameters	Value
Length: L (mm)	20
Thickness: $2h$ (mm)	0.4
Width: w (mm)	1
Initial crack length: a_0 (mm)	10
Young's modulus: E_1 (GPa)	135
Shear modulus: G_{13} (GPa)	5.7
Interfacial normal strength: t_n^0 (MPa)	50
Mode I interfacial fracture toughness: \mathcal{G}_{Ic} (N/mm)	0.4
Penalty stiffness of cohesive elements: K (N/mm ³)	10^6 [43]

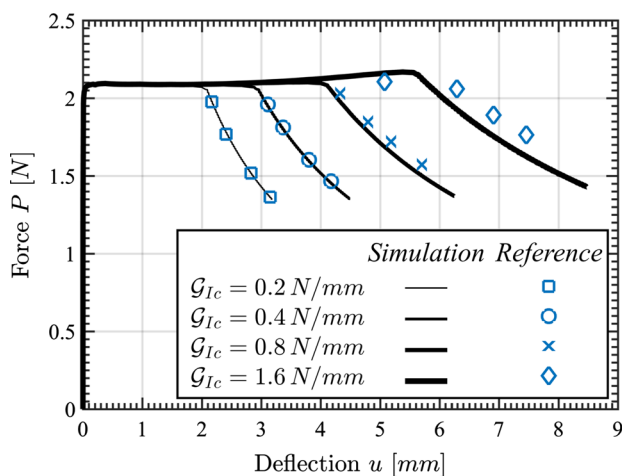
required to track the crack loci. As regards problems studied here, possible scenarios of crack propagation and the simulation in a mesh are shown in Fig. 7. As plotted in Fig. 7a, the crack is propagating in the matrix material and may intersect the lower element in a slantwise manner. According to the edge status variable approach [43], the status of edge #2 changes from *intact* to *broken* while the status of edge #3 to *transitional*. At the *broken* edge, two floating nodes are activated and taken into account in global calculation of stiffness and mass matrices. But for the floating node at the *transitional* edge, its displacements are interpolated by two real nodes at the ends of the edge and condensed out of the global stiffness assembly. Figure 7b illustrates the change to be made on adjacent cohesive element and 0° solid element when the crack approaches the interface. Two floating nodes are activated on the *broken* edge #1 while one is activated on the edge #2 (labeled as *refined*) of two cohesive elements. To preserve compatibility, the adjacent 0° ply element is refined as three triangular elements. In this way, the crack can be

monitored with the local tracking method based on edge status variable.

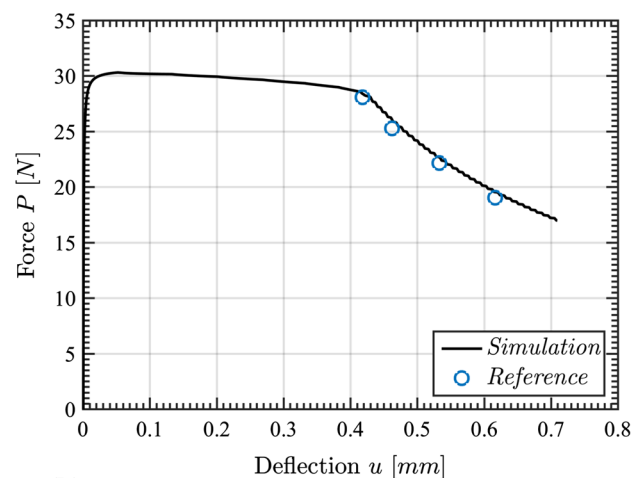
Once the crack location is determined, the solid element or interface element is partitioned into two or more sub-elements by virtue of enriched elements formulated in Sects. 3.2 and 3.3.

5 Representative numerical simulations

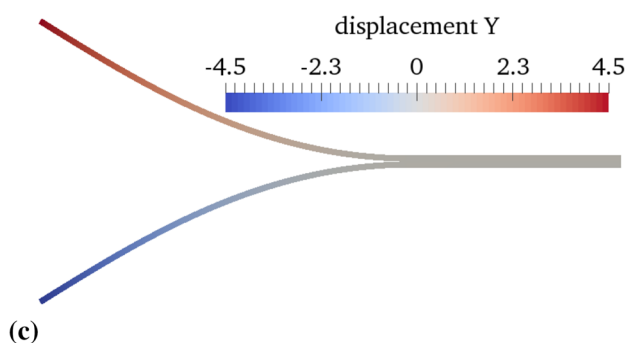
In this section, the performance of the proposed method is illustrated with two numerical simulation examples involving large displacements. Firstly, the problem of buckling-driven delamination is addressed with a beam under axial compression. Secondly, damage propagation in composites subjected to low-velocity impact is modeled with matrix cracking and delamination growth.



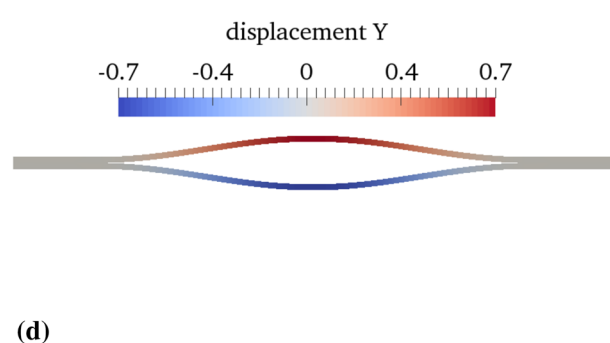
(a)



(b)



(c)



(d)

Fig. 9 Numerical results of compressive load versus transversal deflection (datum of markers refer to [57]): Case-1 (a), Case-2 (b); deformation ($G_{Ic} = 0.4$ N/mm): Case-1 (c), Case-2 (d)

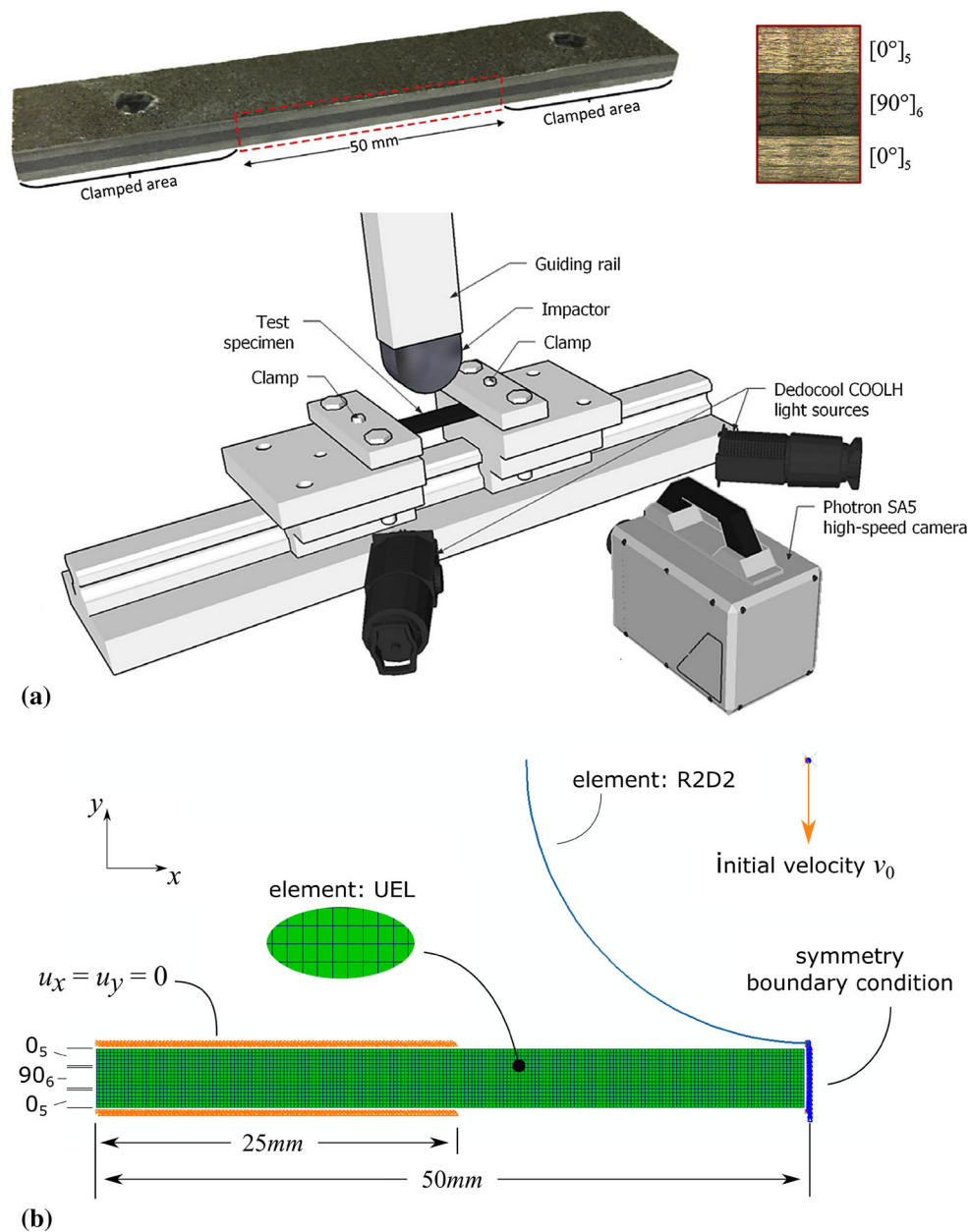


Fig. 10 a Illustration of experimental setup [63]; b numerical model

5.1 Buckling-induced delamination

The problem posed by Allix and Corigliano [57] is chosen herein to verify the method on geometrically nonlinear analysis of delamination in composites. As shown in Fig. 8, two composite beams with predefined initial crack (a. crack on the left for Case-1; b. centrally positioned crack for Case-2) are loaded by a horizontal rightward displacement u . Buckling is triggered by a small perturbation displacement u_0 , which aims at introducing an initial imperfection for post-buckling analysis. Subsequently, mode-I delamination propagates along the interface with the opening of the two

arms of the buckled beam. The geometric dimensions and material properties of the beam are listed in Table 1 [57].

The beam is modeled with solid elements and cohesive elements proposed in the previous section for 0° ply and interface, respectively. A uniform mesh of square elements with side length of 0.05 mm is adopted. In the simulation, the specimens are loaded under displacement control for stable crack propagation. At the first step, an initial symmetric perturbation (small vertical displacement of 6×10^{-4} mm) is applied. A horizontal displacement is imposed continuously in the second step, during which the reaction force P

and the transverse deflection u at point ‘A’ (Fig. 8) could be evaluated.

The influence of fracture energy is studied by simulations of Case-1 with four values of $\mathcal{G}_{Ic} = \{0.2, 0.4, 0.8, 1.6\}$ (N/mm) and a constant value of normal strength t_n^0 . For the example with $\mathcal{G}_{Ic} = 1.6$ (N/mm), the computational time taken is approximately 0.3 CPU-hour on a workstation with processors of Intel® Xeon® X5690 @ 3.47GHz. The four load-displacement ($P - u$) curves are plotted in Fig. 9a and compared with results given in [57]; they show good agreement. The theoretical buckling load of the beam with thickness h is 2.22 N [57]. As shown in Fig. 9a, before the force reaches 2.1 N, the load P increases dramatically while the deflection at point ‘A’ remains small. With the onset of buckling, deflection increases drastically but the force remains the same and then decreases due to delamination propagation. It can be seen from Fig. 9a that a tougher interface postpones the occurrence of delamination. For Case-2 (Fig. 9b), as with Case-1, buckling first occurs, followed by delamination propagation. However, the peak load is larger and the deflection is smaller for Case-2 as shown by the deformed configurations in Fig. 9c, d.

5.2 Low-velocity impact damage

The second chosen example is a dynamic problem of a carbon fiber reinforced composite beam impacted by a cylindrical head [63], originally proposed for the study of failure sequences subjected to low-velocity impact. Unlike the more common semispherical-head impactor, this uniform line-loading approach [64] facilitates monitoring of failure patterns from the side of the composite beam. The impact analysis is simplified as a two-dimensional case, which makes it suitable to benchmark the current computational method. The experimental setup is given in Fig. 10a, where the size of the beam is 100 mm \times 17 mm \times 4.8 mm and the diameter of the impactor is 40 mm. The beam is made from Hexcel 913C-HTS carbon-epoxy unidirectional prepregs with a cross-ply lay-up sequence $[0_5/90_3]_s$ and the material properties are listed in Table 2 [63].

Taking into account symmetric boundary conditions, the FE model as shown in Fig. 10b is adopted. The impactor is discretized with 2D rigid elements R2D2 in ABAQUS® [62] and the mass of this half model of the impactor is 392.5 g. The specimen is modeled with three types of elements (ABAQUS® UEL) developed for 0° plies, 90° plies and interfaces, as shown in Fig. 6. A uniform mesh size of 0.25 mm along the length of the beam is used while each ply is modeled with a single element of 0.3 mm through thickness. Contact interactions are defined between the outer surface of the impactor and the top surface of the beam. The bottom and top surfaces of the left half of the beam model are constrained. An initial downward velocity $v_0 = 4.43$ m/s is

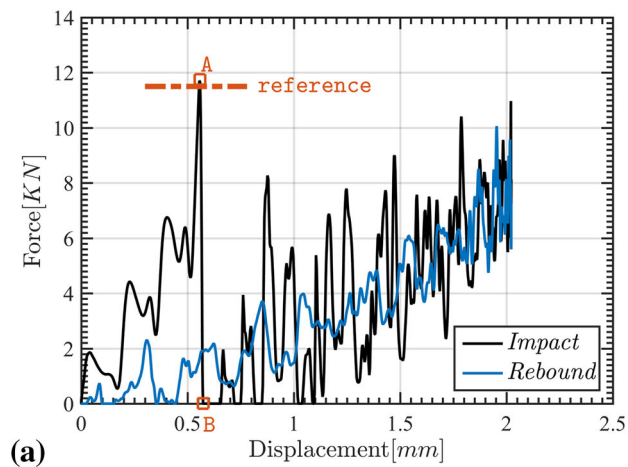
Table 2 Material properties of Hexcel 913C-HTS carbon-epoxy composites [63]

Property	Value
Longitudinal Young’s modulus: E_1 (GPa)	135
Transverse Young’s modulus: E_2, E_3 (GPa)	9.2
Shear modulus: G_{12}, G_{13} (GPa)	5.5
Shear modulus: G_{23} (GPa)	4.5
Poisson’s ratio: ν_{12}, ν_{13}	0.30
Poisson’s ratio: ν_{23}	0.45
Density: ρ (kg/m ³)	1780
Transverse tensile strength: f_n (MPa)	60
Interfacial normal strength: t_n^0 (MPa)	105
Interfacial shear strength: t_t^0 (MPa)	105
Mode I interfacial fracture toughness: \mathcal{G}_{Ic} (N/mm)	0.26
Mode II interfacial fracture toughness: \mathcal{G}_{IIc} (N/mm)	0.84
Penalty stiffness of cohesive elements: K (N/mm ³)	10^6 [43]

imposed on the the impactor. Implicit dynamic analysis is used [62] and the time step is taken as 0.003 s. The total CPU time consumed is about 1.8 h.

The computed force-displacement curve (contact force between the impactor and the beam versus the downward distance of the impactor) is given in Fig. 11a. No experimental force-displacement data from Ref. [63] is available for comparison. During the initial elastic loading, periodic oscillations are observed in the curve due to wave reflections. When the curve reaches point ‘A’, several diagonal matrix cracks initiate in the 90° plies as shown by results from experiment and simulation in Fig. 11b. These are caused by transverse shear stress and usually denoted as “shear cracks” in the literature [65]. According to the Rankine criterion, the maximum principal stress determines the crack onset and direction. In simulation, it is observed that the two initial cracks traverse the 90° plies through the thickness, resulting in smooth and straight crack loci. The location of these matrix cracks from the center of impact varies between 18.75–21.25 mm and is close to experimental observations (average distance 18.1 mm). The average angles between the crack and the horizontal line measured in experiment and simulation are 49° and 45°, respectively, indicating a shear dominated failure. At the same time, the force reaches the peak value 11.4 KN, which coincides with the results (11.7 KN) from the simulation with continuum damage model [63]. Shortly after crack initiation, the load suddenly drops to almost zero at point ‘B’. The lower interface crack propagates away from the center while the upper one propagates toward to the impact point and significant crack openings can be observed. After point ‘B’ in Fig. 11a, the contact force increases again, during which larger fluctuations can be observed as a result of the delamination and matrix cracks. When the residual

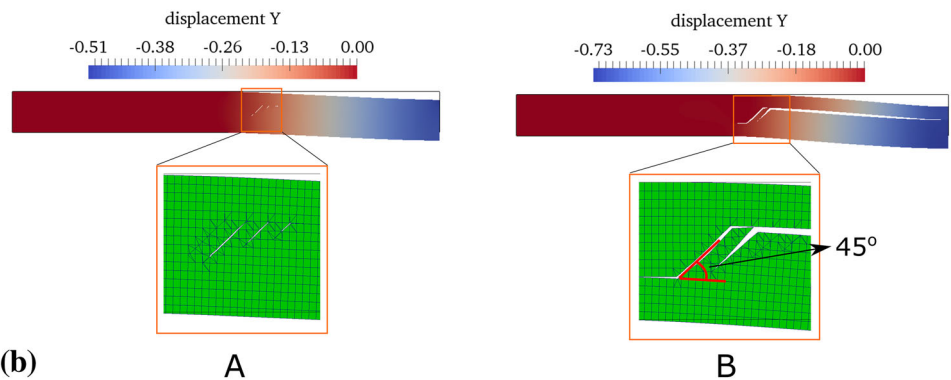
Fig. 11 Comparisons between results from simulation and experiment [63]: **a** Load displacement curves; **b** typical failure patterns (at point A & B)



Experiment



Simulation



kinetic energy of the impactor is consumed completely, the impactor starts rebounding and contact force decreases gradually.

5.3 Discussions

The simulation in Sect. 5.1 has illustrated the phenomenon of geometrical instability and accompanying delamination propagation, which are captured by a geometrically nonlinear formulation of FNM. A comparative study of nonlinear effects on the second example is conducted by comparing the nonlinear results with the results given by a geometrically linear analysis. During the impact process, the two load-displacement curves are plotted in Fig. 12a, where only the loading part is shown. It can be seen that two curves for the

elastic loading stage is the same and the peak load predicted by the linear analysis is slightly higher. This is unsurprising due to the relatively small deformations, for which the effect of geometric non-linearity is not important. However, the difference between the two curves increases with further deformation. As seen from Fig. 12a and the results at maximum deformation point listed in Table 3, the contact force predicted by the nonlinear analysis is larger and the maximum displacement is smaller compared with the result by the linear formulation.

Furthermore, a subsequent virtual test for CAI (compression after impact) modeling, in which a compressive load was applied at the left end of the laminate (the case in Fig. 8b) with the impact damage already embedded in the model, was conducted in a quasi-static analysis. Since the damage in 0°

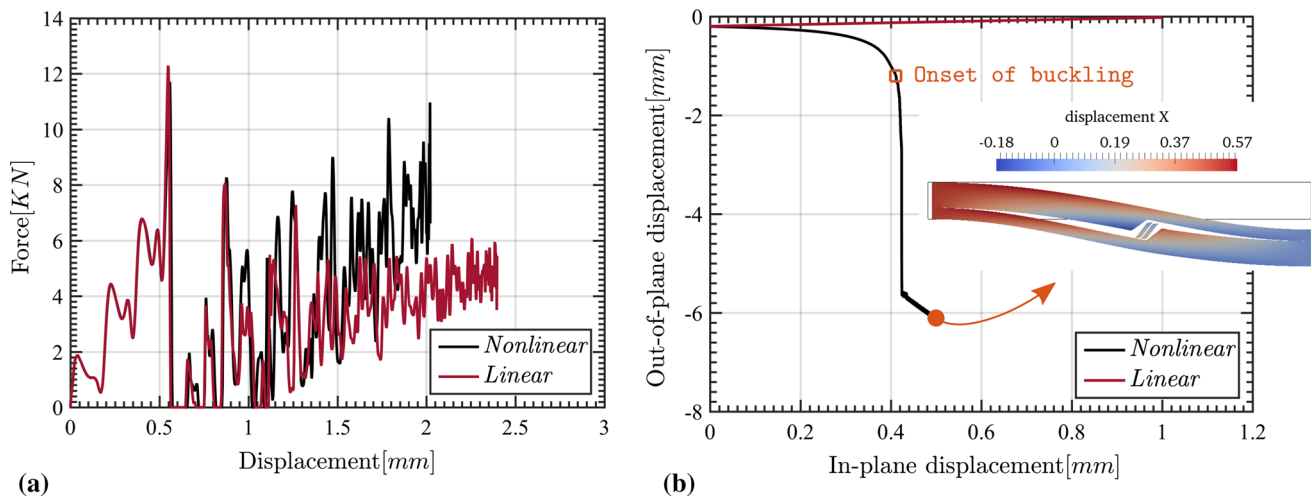


Fig. 12 Comparisons between results given by geometrically nonlinear and linear formulations: **a** Load-displacement curves during impact; **b** transversal deflection versus applied in-plane displacement during compression after impact

Table 3 Comparisons of results at maximum deformation point from the nonlinear and linear analyses

	Nonlinear analysis	Linear analysis
Contact force (kN)	10.84	5.95
Displacement (mm)	2.02	2.38

plies is not considered in the current formulation, the permanent indentation after impact is not captured here. Therefore, only a downward perturbation (0.2 mm) in Fig. 8b is applied. The results of transverse deflection versus applied displacement of the laminate are plotted in Fig. 12b. It can be seen in the nonlinear analysis results that buckling starts when the applied displacement reaches 0.4 mm, after which the generated matrix cracks and delaminations due to low-velocity impact continue propagating and the final failure pattern is shown in Fig. 12b. However, the linear analysis fails to capture the damage growth in laminates subjected to CAI. The out-of-plane deformation decreases to zero gradually and only axial compressive deformation can be observed finally.

6 Conclusion

In this work, the floating node method for modeling of strong discontinuities in laminated composites and their interactions in the large deformation range was developed. The jump in the deformation map and corresponding deformation gradient were captured with formulated enriched solid elements and enriched cohesive elements, which are used for the analysis of matrix cracking and delamination, respectively. A mixed-mode cohesive model was adopted for the simulation of the behavior of these cracks. Two representative numer-

ical examples were presented to verify the performance of the proposed methods. Good agreement with referenced results from literature were obtained in terms of both load-displacement curves and crack propagation patterns. The first example shows a verification of the formulation in modeling buckling problems with geometric non-linearity. Buckling initiates, followed by delamination propagation due to transverse deformation. The second example examines the capability of this method in modeling coupled dynamic failure mechanisms in composites subjected to low-velocity impact. Matrix cracking is firstly observed during the early stage and diagonal matrix cracks are captured with the Rankine criterion. With these cracks approaching interfaces between plies, delaminations along the upper and lower interfaces are then induced and propagate in opposite directions.

Comparisons between results by linear and nonlinear analyses have shown that the geometric non-linearity is not significant at the damage initiation of a coupon-level specimen since the deformation is usually small. But it is important for modeling accurately further deformation and compressive failure with buckling. Therefore, considering geometric non-linearity is necessary for a general damage modeling of composites. Although the current work only shows 2D examples, the proposed method can be extended for three dimensional analysis. One significant potential application is discrete crack analysis of 3D failure patterns in low- and medium-velocity impact of laminated composites [6,7].

Acknowledgements The support of the research scholarship for the first author and the Research Grant (No. R265000523646) from NUS are gratefully acknowledged.

Appendix: Linearization of internal force and cohesive force

Nonlinear problem is usually formulated as linear algebraic equations for *Newton-Raphson* iterative solution. The linearization of force terms contributed by solid element and cohesive element is presented in this section and stiffness matrices are derived. Note that the linearization procedure can be either conducted directly on weak formulation (Eqs. 10, 11) or FE formulation (Eqs. 30, 31). The first approach is more commonly seen in the literature [60,66] and introduced herein.

The linear part of $\delta\mathcal{W}_{int}$ is given by

$$L[\delta\mathcal{W}_{int}]_{u=\underline{u}} = \delta\mathcal{W}_{int}(\underline{u}, \delta\mathbf{u}) + \Delta(\delta\mathcal{W}_{int}(\underline{u}, \delta\mathbf{u})) \tag{43}$$

where

$$\begin{aligned} \Delta(\delta\mathcal{W}_{int}(\underline{u}, \delta\mathbf{u})) &= \int_{\Omega_0 \setminus \Gamma_0} [\delta\mathbf{E} : \mathbb{D} : \Delta\mathbf{E} \\ &+ \text{Grad } \Delta\mathbf{u} \cdot \underline{\mathbf{S}} : \text{Grad } \delta\mathbf{u}] dV. \end{aligned} \tag{44}$$

\square denotes variables at an equilibrium deformation state. With similar discretization given in Eq. (23), the linearization of the internal force at element level is given by

$$\Delta(\mathbf{F}_{int}^e) = (\underline{\mathbf{K}}_{mat}^e + \underline{\mathbf{K}}_{geo}^e) \Delta\mathbf{d}^e \tag{45}$$

where the material and geometric contribution to tangent stiffness matrix are given by

$$(\underline{\mathbf{K}}_{mat}^e)_{IJ} = \int_{\Omega_0^e} (\underline{\mathbf{B}}_L^e)^T)_I \{\mathbb{D}\} (\underline{\mathbf{B}}_L^e)_J dV \tag{46}$$

$$(\underline{\mathbf{K}}_{geo}^e)_{IJ} = \int_{\Omega_0^e} (\nabla_X N_I^e \cdot \underline{\mathbf{S}} \cdot \nabla_X N_J^e) \mathbf{I}_2 dV \tag{47}$$

where I and J are indices of nodes.

The linear part of $\delta\mathcal{W}_{coh}$ is given by

$$\begin{aligned} L[\delta\mathcal{W}_{coh}]_{\llbracket \mathbf{u} \rrbracket = \llbracket \underline{\mathbf{u}} \rrbracket} &= \delta\mathcal{W}_{coh}(\llbracket \underline{\mathbf{u}} \rrbracket, \llbracket \delta\mathbf{u} \rrbracket) \\ &+ \Delta(\delta\mathcal{W}_{coh}(\llbracket \underline{\mathbf{u}} \rrbracket, \llbracket \delta\mathbf{u} \rrbracket)) \end{aligned} \tag{48}$$

where the second term consists of three parts

$$\begin{aligned} &\int_{\Gamma} \{ \llbracket \delta\mathbf{u} \rrbracket \cdot \underline{\mathbf{t}}_{c, \llbracket \underline{\mathbf{u}} \rrbracket} \cdot \llbracket \Delta\mathbf{u} \rrbracket + \llbracket \delta\mathbf{u} \rrbracket \cdot \underline{\mathbf{t}}_{c, \mathbf{n}} \cdot \Delta\mathbf{n} \} da \\ &+ \int_{\Gamma} \llbracket \delta\mathbf{u} \rrbracket \cdot \underline{\mathbf{t}}_c \Delta da \end{aligned} \tag{49}$$

where $\underline{\mathbf{t}}_{c, \llbracket \underline{\mathbf{u}} \rrbracket}$ and $\underline{\mathbf{t}}_{c, \mathbf{n}}$ are tangent moduli with respect to $\llbracket \underline{\mathbf{u}} \rrbracket$ and \mathbf{n} . Similarly, the tangent stiffness matrix can also be given

as

$$(\underline{\mathbf{K}}_{mat}^e)_{IJ} = \int_{\Gamma^e} L_I^e \underline{\mathbf{t}}_{c, \llbracket \underline{\mathbf{u}} \rrbracket} L_J^e da \tag{50}$$

$$\begin{aligned} (\underline{\mathbf{K}}_{geo}^e)_{IJ} &= \int_{\Gamma^e} [L_I^e \underline{\mathbf{t}}_{c, \mathbf{n}} \cdot \underline{\mathbf{G}} \cdot \frac{1}{2} \nabla_X \bar{N}_J^e \\ &+ L_I^e \underline{\mathbf{t}} \otimes \underline{\mathbf{A}} \cdot \frac{1}{2} \nabla_X \bar{N}_J^e] da \end{aligned} \tag{51}$$

where $\underline{\mathbf{G}} = -\mathbf{n} \cdot \mathbf{I} \otimes \mathbf{F}^{-T} + \mathbf{n} \otimes \mathbf{n} \otimes \mathbf{n} \cdot \mathbf{F}^{-T}$, $\underline{\mathbf{A}} = (\mathbf{I} - \mathbf{n} \otimes \mathbf{n}) \cdot \mathbf{F}^{-T}$, \mathbf{I} is the second order unit tensor.

The stiffness matrices of enriched elements can be obtained as an assembly of the tangent matrices by sub-elements. Note that consistent linearization is conducted here to achieve quadratic convergence. However, the tangent stiffness matrix can lose its symmetry due to the geometric contribution, e.g., Eq. (51). To utilize the symmetric solvers, those terms can be ignored without affecting the accuracy [67].

References

1. Liu PF, Zheng JY (2010) Recent developments on damage modeling and finite element analysis for composite laminates: a review. *Mater Des* 31(8):3825–3834
2. Orifici AC, Herszberg I, Thomson RS (2008) Review of methodologies for composite material modelling incorporating failure. *Compos Struct* 86(1):194–210
3. Zhi J, Zhao LB, Zhang JY, Liu ZL (2016) A numerical method for simulating the microscopic damage evolution in composites under uniaxial transverse tension. *Appl Compos Mater* 23(3):255–269
4. Nairn JA (2000) 2.12-matrix microcracking in composites. In: Kelly A, Zweben C (eds) *Comprehensive composite materials*. Pergamon, Oxford, pp 403–432
5. Tay TE (2003) Characterization and analysis of delamination fracture in composites: an overview of developments from 1990 to 2001. *Appl Mech Rev* 56(1):1–32
6. Abir MR, Tay TE, Ridha M, Lee HP (2017) Modelling damage growth in composites subjected to impact and compression after impact. *Compos Struct* 168:13–25
7. Abir MR, Tay TE, Ridha M, Lee HP (2017) On the relationship between failure mechanism and compression after impact (cai) strength in composites. *Compos Struct* 182:242–250
8. Yang QD, Schesser D, Niess M, Wright P, Mavrogordato MN, Sinclair I, Spearing SM, Cox BN (2015) On crack initiation in notched, cross-plyed polymer matrix composites. *J Mech Phys Solids* 78:314–332
9. de Borst R, Remmers JJC, Needleman A, Abellan MA (2004) Discrete vs smeared crack models for concrete fracture: bridging the gap. *Int J Numer Anal Methods Geomech* 28(7–8):583–607
10. Jirásek M (2000) Damage and smeared crack models. In: Hofstetter G, Meschke G (eds) *Numerical modeling of concrete cracking*. Springer, Berlin, pp 1–49
11. Peerlings RHJ, Geers MGD, de Borst R, Brekelmans WAM (2001) A critical comparison of nonlocal and gradient-enhanced softening continua. *Int J Solids Struct* 38(44):7723–7746
12. Poh LH, Sun G (2017) Localizing gradient damage model with decreasing interactions. *Int J Numer Methods Eng* 110(6):503–522
13. Miehe C, Hofacker M, Welschinger F (2010) A phase field model for rate-independent crack propagation: Robust algorithmic imple-

- mentation based on operator splits. *Comput Methods Appl Mech Eng* 199(45–48):2765–2778
14. Verhoosel CV, de Borst R (2013) A phase-field model for cohesive fracture. *Int J Numer Methods Eng* 96(1):43–62
 15. de Borst R, Verhoosel CV (2016) Gradient damage vs phase-field approaches for fracture. *Comput Methods Appl Mech Eng* 312:78–94
 16. de Pouplana I, Oñate E (2016) Combination of a non-local damage model for quasi-brittle materials with a mesh-adaptive finite element technique. *Finite Elements Anal Des* 112:26–39
 17. Patil RU, Mishra BK, Singh IV (2018) An adaptive multiscale phase field method for brittle fracture. *Comput Methods Appl Mech Eng* 329:254–288
 18. Moës N, Belytschko T (2002) Extended finite element method for cohesive crack growth. *Eng Fract Mech* 69(7):813–833
 19. Oliver J, Huespe AE, Sanchez PJ (2006) A comparative study on finite elements for capturing strong discontinuities: E-FEM vs X-FEM. *Comput Methods Appl Mech Eng* 195(37):4732–4752
 20. Hansbo A, Hansbo P (2004) A finite element method for the simulation of strong and weak discontinuities in solid mechanics. *Comput Methods Appl Mech Eng* 193(33):3523–3540
 21. P Jäger (2009) Theory and numerics of three-dimensional strong discontinuities at finite strains. PhD thesis, Technische Universität Kaiserslautern
 22. Song JH, Areias P, Belytschko T (2006) A method for dynamic crack and shear band propagation with phantom nodes. *Int J Numer Methods Eng* 67(6):868–893
 23. Mergheim J, Kuhl E, Steinmann P (2005) A finite element method for the computational modelling of cohesive cracks. *Int J Numer Methods Eng* 63(2):276–289
 24. Chau-Dinh T, Zi G, Lee PS, Rabczuk T, Song JH (2012) Phantom-node method for shell models with arbitrary cracks. *Comput Struct* 92:242–256
 25. Gasser TC, Holzapfel GA (2003) Geometrically non-linear and consistently linearized embedded strong discontinuity models for 3d problems with an application to the dissection analysis of soft biological tissues. *Comput Methods Appl Mech Eng* 192(47):5059–5098
 26. Fagerström M, Larsson R (2006) Theory and numerics for finite deformation fracture modelling using strong discontinuities. *Int J Numer Methods Eng* 66(6):911–948
 27. Mergheim J, Steinmann P (2006) A geometrically nonlinear FE approach for the simulation of strong and weak discontinuities. *Comput Methods Appl Mech Eng* 195(37):5037–5052
 28. Armero F, Linder C (2008) New finite elements with embedded strong discontinuities in the finite deformation range. *Comput Methods Appl Mech Eng* 197(33):3138–3170
 29. Matzenmiller A, Lubliner J, Taylor RL (1995) A constitutive model for anisotropic damage in fiber-composites. *Mech Mater* 20(2):125–152
 30. Maimí P, Camanho PP, Mayugo JA, Dávila CG (2007) A continuum damage model for composite laminates: part I-constitutive model. *Mech Mater* 39(10):897–908
 31. Reinoso J, Catalanotti G, Blázquez A, Areias P, Camanho PP, París F (2017) A consistent anisotropic damage model for laminated fiber-reinforced composites using the 3D-version of the Puck failure criterion. *Int J Solids Struct* 126:37–53
 32. Van der Meer FP, Sluys LJ (2009) A phantom node formulation with mixed mode cohesive law for splitting in laminates. *Int J Fract* 158(2):107
 33. Van der Meer FP, Sluys LJ (2010) Mesh-independent modeling of both distributed and discrete matrix cracking in interaction with delamination in composites. *Eng Fract Mech* 77(4):719–735
 34. Van der Meer FP, Sluys LJ, Hallett SR, Wisnom MR (2012) Computational modeling of complex failure mechanisms in laminates. *J Compos Mater* 46(5):603–623
 35. Ahmed A, Sluys LJ (2013) A three-dimensional progressive failure model for laminated composite plates subjected to transverse loading. *Eng Fract Mech* 114:69–91
 36. Ling DS, Yang QD, Cox B (2009) An augmented finite element method for modeling arbitrary discontinuities in composite materials. *Int J Fract* 156(1):53–73
 37. Zhou ZQ, Fang XJ, Cox BN, Yang QD (2010) The evolution of a transverse intra-ply crack coupled to delamination cracks. *Int J Fract* 165(1):77–92
 38. Fang XJ, Yang QD, Cox BN, Zhou ZQ (2011) An augmented cohesive zone element for arbitrary crack coalescence and bifurcation in heterogeneous materials. *Int J Numer Methods Eng* 88(9):841–861
 39. Fang XJ, Zhou ZQ, Cox BN, Yang QD (2011) High-fidelity simulations of multiple fracture processes in a laminated composite in tension. *J Mech Phys Solids* 59(7):1355–1373
 40. Tay TE, Sun XS, Tan VBC (2014) Recent efforts toward modeling interactions of matrix cracks and delaminations: an integrated XFEM-CE approach. *Adv Compos Mater* 23(5–6):391–408
 41. Hu XF, Chen BY, Tirvaudey M, Tan VBC, Tay TE (2016) Integrated XFEM-CE analysis of delamination migration in multi-directional composite laminates. *Compos Part A Appl Sci Manuf* 90:161–173
 42. Chen BY, Pinho ST, De Carvalho NV, Baiz PM, Tay TE (2014) A floating node method for the modelling of discontinuities in composites. *Eng Fract Mech* 127:104–134
 43. Chen BY, Tay TE, Pinho ST, Tan VBC (2016) Modelling the tensile failure of composites with the floating node method. *Comput Methods Appl Mech Eng* 308:414–442
 44. Chen BY, Tay TE, Pinho ST, Tan VBC (2017) Modelling delamination migration in angle-ply laminates. *Compos Sci Technol* 142:145–155
 45. Iarve EV, Gurvich MR, Mollenhauer DH, Rose CA, Dávila CG (2011) Mesh-independent matrix cracking and delamination modeling in laminated composites. *Int J Numer Methods Eng* 88(8):749–773
 46. Zhao LB, Zhi J, Zhang JY, Liu ZL, Hu N (2016) XFEM simulation of delamination in composite laminates. *Compos Part A Appl Sci Manuf* 80:61–71
 47. Higuchi R, Okabe T, Nagashima T (2017) Numerical simulation of progressive damage and failure in composite laminates using XFEM/CZM coupled approach. *Compos Part A Appl Sci Manuf* 95:197–207
 48. Li XL, Chen JY (2016) An extended cohesive damage model for simulating multicrack propagation in fibre composites. *Compos Struct* 143:1–8
 49. Li DH, Zhang X, Sze KY, Liu Y (2016) Extended layerwise method for laminated composite plates with multiple delaminations and transverse cracks. *Comput Mech* 58(4):657–679
 50. Qiu Y, Crisfield MA, Alfano G (2001) An interface element formulation for the simulation of delamination with buckling. *Eng Fract Mech* 68(16):1755–1776
 51. Reinoso J, Paggi M, Blázquez A (2017) A nonlinear finite thickness cohesive interface element for modeling delamination in fibre-reinforced composite laminates. *Compos Part B Eng* 109:116–128
 52. Škec L, Jelenić G (2017) Geometrically non-linear multi-layer beam with interconnection allowing for mixed-mode delamination. *Eng Fract Mech* 169:1–17
 53. Wells GN, de Borst R, Sluys LJ (2002) A consistent geometrically non-linear approach for delamination. *Int J Numer Methods Eng* 54(9):1333–1355
 54. Malvern LE (1969) Introduction to the mechanics of a continuous medium. Prentice Hall, Upper Saddle River
 55. Bonet J, Burton AJ (1998) A simple orthotropic, transversely isotropic hyperelastic constitutive equation for large strain computations. *Comput Methods Appl Mech Eng* 162(1–4):151–164
 56. Bathe KJ (2006) Finite element procedures. Prentice Hall, Upper Saddle River

57. Allix O, Corigliano A (1999) Geometrical and interfacial nonlinearities in the analysis of delamination in composites. *Int J Solids Struct* 36(15):2189–2216
58. Turon A, Camanho PP, Costa J, Dávila CG (2006) A damage model for the simulation of delamination in advanced composites under variable-mode loading. *Mech Mater* 38(11):1072–1089
59. Overgaard LCT, Lund E, Camanho PP (2010) A methodology for the structural analysis of composite wind turbine blades under geometric and material induced instabilities. *Comput Struct* 88(19):1092–1109
60. Wriggers P (2008) *Nonlinear finite element methods*. Springer, Berlin
61. Hilber HM, Hughes TJR, Taylor RL (1977) Improved numerical dissipation for time integration algorithms in structural dynamics. *Earthq Eng Struct Dyn* 5(3):283–292
62. Dassault Systemes Simulia Corp (2016) *Abaqus user's manual*
63. Topac OT, Gozluklu B, Gurses E, Coker D (2017) Experimental and computational study of the damage process in CFRP composite beams under low-velocity impact. *Compos Part A Appl Sci Manuf* 92:167–182
64. Choi HY, Downs RJ, Chang FK (1991) A new approach toward understanding damage mechanisms and mechanics of laminated composites due to low-velocity impact: Part I experiments. *J Compos Mater* 25(8):992–1011
65. Richardson MOW, Wisheart MJ (1996) Review of low-velocity impact properties of composite materials. *Compos Part A Appl Sci Manuf* 27(12):1123–1131
66. Mergheim J (2006) *Computational modeling of strong and weak discontinuities*. PhD thesis, University of Kaiserslautern
67. Reinoso J, Paggi M (2014) A consistent interface element formulation for geometrical and material nonlinearities. *Comput Mech* 54(6):1569–1581

Publisher's Note Springer Nature remains neutral with regard to jurisdictional claims in published maps and institutional affiliations.